The Astronomical Journal, 157:233 (11pp), 2019 June https://doi.org/10.3847/1538-3881/ab16cd

The Composite Nature of Dust-obscured Galaxies (DOGs) at $z \sim 2$–3 in the COSMOS Field. II. The AGN Fraction

Laurie A. Riguccini[1,22], Ezequiel Treister[2], Karin Menéndez-Delmestre[1], Carolin Cardamone[3], Francesca Civano[4], Thiago S. Gonçalves[1], Guenther Hasinger[5], Anton M. Koekemoer[6], Giorgio Lanzuisi[7,8], Emeric Le Floc'h[9], Elisabeta Lusso[10], Dieter Lutz[11], Stefano Marchesi[12], Takamitsu Miyaji[13], Francesca Pozzi[8,14], Claudio Ricci[2,15,16,17], Giulia Rodighiero[18], Mara Salvato[19], Dave Sanders[5], Kevin Schawinski[20], and Hyewon Suh[21]
[1] Observatório do Valongo, Universidade Federal do Rio de Janeiro, Ladeira do Pedro Antônio 43, Saúde, Rio de Janeiro, RJ 20080-090, Brazil
riguccini@astro.ufrj.br
[2] Instituto de Astrofísica, Facultad de Física, Pontificia Universidad Católica de Chile, Casilla 306, Santiago 22, Chile
[3] Math and Science Department, Wheelock College, Boston, MA 02215, USA
[4] Harvard-Smithsonian Center for Astrophysics, Cambridge, MA 02138, USA
[5] Institute for Astronomy, University of Hawaii, 2680 Woodlawn Drive, Honolulu, HI 96822, USA
[6] Space Telescope Science Institute, 3700 San Martin Drive, Baltimore, MD 21218, USA
[7] Dipartimento di Fisica e Astronomia, Universita di Bologna, viale Berti Pichat 6/2, I-40127 Bologna, Italy
[8] INAF Osservatorio Astronomico di Bologna, Via Ranzani 1, I-40127, Bologna, Italy
[9] Laboratoire AIM, CEA/DSM-CNRS-Université Paris Diderot, IRFU/Service d'Astrophysique, Bât.709, CEA-Saclay, F-91191 Gif-sur-Yvette Cedex, France
[10] Centre for Extragalactic Astronomy, Department of Physics, Durham University, South Road, Durham, DH1 3LE, UK
[11] Max-Planck-Institut für extraterrestrische Physik, Postfach 1312, Giessenbachstrasse 1, D-85741 Garching, Germany
[12] Department of Physics & Astronomy, Clemson University, Clemson, SC 29634, USA
[13] Universidad Nacional Autónoma de México sede Ensenada, Carret. Tijuna-Ensenada Km 103, Ensenada 22860, BC, Mexico
[14] Dipartimento di Fisica e Astronomia, Universitá degli Studi di Bologna, Viale Berti Pichat 6/2, I-40127 Bologna, Italy
[15] Núcleo de Astronomía de la Facultad de Ingeniería, Universidad Diego Portales, Av. Ejército Libertador 441, Santiago, Chile
[16] Kavli Institute for Astronomy and Astrophysics, Peking University, Beijing 100871, People's Republic of China
[17] Chinese Academy of Sciences South America Center for Astronomy and China-Chile Joint Center for Astronomy, Camino El Observatorio 1515, Las Condes, Santiago, Chile
[18] Dipartimento di Fisica e Astronomia "G. Galilei", Universita di Padova, Vicolo dell Osservatorio 3, I-35122, Italy
[19] Max-Planck-Institute für Plasma Physics, Boltzmann Strasse 2, Garching D-85748, Germany
[20] Institute for Astronomy, Department of Physics, ETH Zurich, Wolfgang-Pauli-Strasse 27, CH-8093 Zurich, Switzerland
[21] Subaru Telescope, National Astronomical Observatory of Japan, 650 North A'ohoku Place, Hilo, HI 96720, USA
Received 2018 July 19; revised 2019 March 20; accepted 2019 April 5; published 2019 May 21

Abstract

We present the X-ray properties of 108 Dust-Obscured Galaxies (DOGs; $F_{24\,\mu m}/F_R > 1000$) in the COSMOS field, all of which are detected in at least three far-infrared bands with the *Herschel* Observatory. Out of the entire sample, 22 are individually detected in the hard 2–8 keV X-ray band by the *Chandra* COSMOS Legacy survey, allowing us to classify them as AGN. Six (27%) of them are Compton-thick AGN candidates with column densities $N_H > 10^{24}$ cm^{-2}, while 15 are moderately obscured AGNs with $10^{22} < N_H < 10^{24}$ cm^{-2}. Additionally, we estimate AGN contributions to the IR luminosity (8–1000 μm rest-frame) greater than 20% for 19 DOGs based on SED decomposition using *Spitzer*/MIPS 24 μm and the five *Herschel* bands (100–500 μm). Only 7 of these are detected in X-rays individually. We performed an X-ray stacking analysis for the 86 undetected DOGs. We find that the AGN fraction in DOGs increases with 24 μm flux and that it is higher than that of the general 24 μm population. However, no significant difference is found when considering only X-ray detections. This strongly motivates the combined use of X-ray and far-IR surveys to successfully probe a wider population of AGNs, particularly for the most obscured ones.

Key words: cosmology: observations – galaxies: high-redshift – infrared: galaxies

1. Introduction

Pioneering work with the *Infrared Astronomical Satellite* and the *Infrared Space Observatory* (*ISO*) established that at low redshifts the most luminous infrared (IR) sources tend to be increasingly dominated by active galactic nuclei (AGN; Genzel et al. 1998; Lutz et al. 1998). However, at higher redshifts the high luminosity of ultraluminous IR galaxies (ULIRGs; $L_{IR} > \times 10^{12}\,L_{\odot}$) is not yet fully understood and significant diversity in the AGN-to-starburst ratio (e.g., Joseph 1999; Sanders 1999; Desai et al. 2007; Menéndez-Delmestre et al. 2009; Sani et al. 2010; Petric et al. 2011; Pozzi et al. 2012) remains a critical difficulty in our understanding of these sources. In an effort to address this and other questions, Dey et al. (2008) put forward color-based criteria to efficiently define a statistically significant sample of dusty ULIRGs at $z \sim 1.5$–3. By taking advantage of the unprecedented sensitivity and angular resolution at IR wavelengths of the *Spitzer Space Telescope*, they selected a population of optically faint ($22 < R < 27$) and mid-IR bright ($F_{24\,\mu m} > 0.3$ mJy) "Dust Obscured Galaxies" (DOGs), defined as those sources having $F_{24\,\mu m}/F_R > 1000$.

The efficient selection of dust-obscured sources at high redshifts also had great impact on the search for hidden AGNs. Although X-ray surveys are a powerful tool to select unobscured and mildly obscured AGNs, the current census of actively growing supermassive black holes remains far from complete (e.g., Treister et al. 2004; Worsley et al. 2005; Page et al. 2006; Tozzi et al. 2006; Fiore et al. 2009; Juneau et al.

[22] CAPES/BJT Science Without Borders Postdoctoral Fellow, Brazil.

2011, 2013). The most obscured AGNs, in particular the deeply embedded ones, are mostly absent in X-ray surveys. At these high column densities, the attenuation of X-rays is mainly due to Compton-scattering rather than photoelectric absorption; these sources are the so-called "Compton-thick" (CT) AGNs ($N_{\rm H} \simeq 1.5 \times 10^{24}\,{\rm cm}^{-2}$), of which only a few have been identified in the local universe (Burlon et al. 2011; Ricci et al. 2015, and references therein). At higher redshifts, hundreds of CT AGN candidates have been identified in X-rays thanks to XMM and *Chandra* observations at $E < 10$ keV (e.g., Comastri et al. 2011; Feruglio et al. 2011; Brightman et al. 2014; Buchner et al. 2015; Baronchelli et al. 2017) and *NuSTAR* data at higher X-ray energies (e.g., Civano et al. 2015; Mullaney et al. 2015; Lansbury et al. 2017).

While in principle CT sources are just the high obscuration end of the AGN population, recent studies have shown that they might represent a different and fundamental stage in setting up the supermassive black hole (SMBH) growth-galaxy evolution connection. Indeed, Ricci et al. (2017) shows that there is a clear excess in the relative number of CT AGNs in the last stages of major galaxy mergers, consistent with this being one of the early phases of rapid SMBH growth triggered by a major galaxy merger. Furthermore, a significant fraction of missed Compton-thick accretion might hide an important part of the census of SMBH growth across cosmic history. Indeed, a significant fraction of heavily obscured and CT sources are invoked at all redshifts in order to reproduce the observed Cosmic X-ray Background (CXRB) at 20–30 keV (e.g., Comastri et al. 1995; Gilli et al. 2001, 2007; Ueda et al. 2003, 2014; Treister & Urry 2005; Ballantyne et al. 2006). However, the exact number of CT sources required by the CXRB is still heavily debated and ranges from ∼30% (Gilli et al. 2007) to ∼10% (Treister et al. 2009b; Ballantyne et al. 2011). Hence, determining the space density of CT AGNs remains a critical open issue in our understanding of the role of SMBH for galaxy evolution. Although a large proportion of the obscured AGN population still remains undetected, these objects can already account for a significant fraction of the total SMBH growth (∼70%; Treister & Urry 2005). Indeed, AGN synthesis models that can explain the spectral shape and intensity of the CXRB predict a large volume density of heavily obscured and CT AGNs to reconcile the "active" and "relic" SMBH mass functions (e.g., Gilli et al. 2001, 2007; Marconi et al. 2004; Treister et al. 2004; Treister & Urry 2005; Akylas et al. 2012).

Since it is clear then that X-ray surveys are not sufficient to probe the complete AGN population, alternative selection techniques have been developed. Recent work by Riguccini et al. (2015) showed that a subsample of DOGs with far-IR (100–500 μm) detection have a significant contribution from AGN activity at higher luminosities (Riguccini et al. 2015). This is consistent with recent work on mid-to-far-IR Spectral Energy Distributions (SEDs) of luminous AGNs that have found that a higher AGN contribution in the far-IR, particularly at high AGN luminosities (e.g., Symeonidis et al. 2016; Symeonidis 2017). Because they are selected based on their far-IR output—i.e., at longer wavelengths than the AGNs selected by near-through-mid IR surveys—far-IR selected DOGs can potentially represent a distinctly defined population of AGN candidates.

Previous studies (e.g., Fiore et al. 2009; Treister et al. 2009a) have focused on selecting sizable samples of high luminosity CT AGNs to measure accurately their volume density and to understand whether their obscuration properties are similar to those of lower luminosity AGNs. In this work we adopt the following approach: based on a far-IR selection of DOGs with information on their AGN contribution (from a far-IR perspective) we exploit the *Chandra* COSMOS Legacy Survey (Civano et al. 2016) to assess the AGN fraction in DOGs using the most recent and exquisite combination of far-IR and X-ray data. Our main aim is to quantify the AGN fraction in this population of far-IR DOGs using a multiwavelength approach based on X-ray flux measurements and broadband SED fitting.

The paper is organized as follows: we describe our data in Section 2 and our results in Section 3. More detailed analysis and discussion are presented in Section 4 while our conclusions are summarized in Section 5. Throughout this paper we assume a ΛCDM cosmology with $H_0 = 70\,{\rm km\,s^{-1}}$, $\Omega_m = 0.3$, and $\Omega_\Lambda = 0.7$. Unless otherwise specified, magnitudes are given in the AB system.

2. Data

2.1. Far-IR

As a reference to build our parent sample, we use the catalogs provided by the PEP and HerMES *Herschel* surveys (Roseboom et al. 2010; Berta et al. 2011) to identify far-IR-selected DOGs in the COSMOS field, detected in at least three of the five *Herschel* bands (see Table 1 for a detailed explanation of the different selections). Those catalogs calculate source fluxes in each of the five *Herschel* bands by performing point-spread function fitting at the positions of the 24 μm detected sources from Le Floc'h et al. (2009). Our total sample hence contains 108 far-IR detected DOGs.

Among our sample of 108 far-IR selected DOGs, 22 sources have spectroscopic redshifts from M. Salvato et al. (2019, in preparation). For the rest of our sample, we use the photometric redshifts determined by Riguccini et al. (2015) for their 95 DOGs based on SED fitting using the optical catalog of Ilbert et al. (2009) to access the photometry of these sources in the optical bands. We reanalyze the AGN contributions for these 22 DOGs using their spectroscopic redshifts, based on the approach described in Riguccini et al. (2015). Figure 1 shows the redshift distribution of our sample of 108 far-IR detected DOGs, which include 22 DOGs with spectroscopic redshifts and 86 DOGs with photometric redshifts.

2.2. X-Ray Data

We use the *Chandra* COSMOS Legacy Survey (Civano et al. 2016) to obtain the X-ray counterparts for the far-IR sources in our sample. The *Chandra* COSMOS Legacy Survey covers a total area of ∼2.2 deg^2, uniformly covering the ∼1.7 deg^2 COSMOS/*HST* field at a ∼160 ks depth, expanding on the deep C-COSMOS area (1.45 versus 0.44 deg^2) by a factor of ∼3 at $\sim 3 \times 10^{16}\,{\rm erg\,cm^{-2}\,s^{-1}}$. The deeper and wider coverage of the *Chandra* COSMOS Legacy survey compared to previous X-ray observations of the COSMOS field (e.g., Brusa et al. 2007, 2010; Salvato et al. 2009) allows us to detect new X-ray DOGs that have been missed by previous X-ray surveys.

From a two arcsecond cross-match between the 108 far-IR detected DOGs and the *Chandra* COSMOS Legacy data (Civano et al. 2016) we identify X-ray counterparts for 22 of the sources in our sample, with a median X-ray flux of

Table 1
Number of Sources and Characteristics of Each Selection Described in This Paper

108	DOGs with $F_{24\ \mu m} > 80$ μJy and with a 3σ detection in the 2 PACS bands and with a 3σ detection in at least one of the three SPIRE bands Sample used for the remainder of the paper Hereafter far-IR DOGs
19	far-IR AGN DOGs following the far-IR SED-fitting analysis from Riguccini et al. (2015)
83	far-IR DOGs with $R - K > 2.79$ (e.g., Fiore et al. 2008, 2009)
2	far-IR AGN DOGs but with $R - K < 2.79$
22	far-IR DOGs with an X-ray detection in the *Chandra* COSMOS Legacy survey (Civano et al. 2016)
7	far-IR DOGs with an X-ray detection in the *Chandra* COSMOS Legacy survey (Civano et al. 2016) have been classified as AGN DOGs following the same procedure than in Riguccini et al. (2015)
6	potential Compton-thick AGN ($N_H > 10^{24}$ cm^{-2}) but only two of them are labeled far-IR AGN DOGs

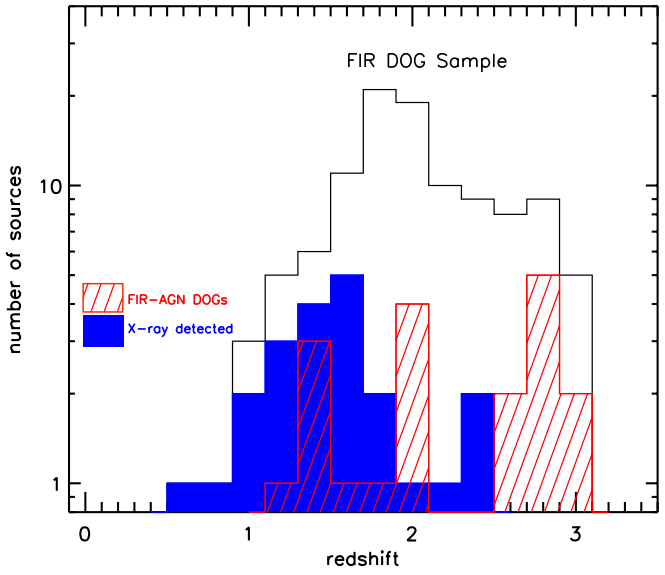

Figure 1. Redshift distribution (22 spectroscopic redshifts and 86 photometric redshifts) for the *Herschel*-selected DOG sample (black histogram). The blue filled histogram shows the subpopulation of DOGs detected in X-rays with the COSMOS *Chandra* Legacy Survey, while the red hatched histogram shows the subpopulation of DOGs classified as AGNs according to the mid-to-far-IR SED fitting. A KS test performed on these last two distributions indicates that they are drawn from a different parent population with a probability of 6×10^{-3}.

$\sim 10^{-16}$ erg s^{-1} in the soft band (0.5–2 keV). From these 22, 9 are detected in X-rays for the first time thanks to the increased field coverage of the *Chandra* COSMOS Legacy Survey. Riguccini et al. (2015) associated *Herschel* sources with their optical counterparts using Ilbert et al. (2009) and then had access to the ID from Capak et al. (2007); see Riguccini et al. (2015) for details on the matching method. As a sanity check, we cross-matched our results with the multiwavelength catalog (X-ray to near-IR) from Marchesi et al. (2016) and found the same optical ID.

3. Results

3.1. Source Classification

Taking advantage of the far-IR data, the AGN and host galaxy contributions to the total IR flux have been constrained by Riguccini et al. (2015) for 95 out of the 108 far-IR selected DOGs. They use the IDL-based SED-fitting procedure DecompIR, detailed in Mullaney et al. (2011) and combine eight host galaxy templates detailed in Riguccini et al. (2011) with an average AGN template. The validity of this procedure and of the AGN contributions to the IR luminosity obtained are discussed in Mullaney et al. (2011) and Riguccini et al. (2011). Riguccini et al. (2015) found that 75% of the far-IR DOGs are consistent with being dominated by star formation, while 16% have a far-IR output with a significant contribution from an AGN (i.e., contribution from an AGN to the host galaxy >20%). The SED fitting procedure failed for their remaining nine DOGs (out of their sample of 95 DOGs), probably due to uncertainties in redshift, even after probing the different possibilities indicated by the PDF. We note that Riguccini et al. (2015) focused their work on the subsample of DOGs a priori associated with star formation, systematically excluding the <4% of DOGs already-known to be AGNs with X-ray detections down to a flux limit of $S_{0.5-2\,keV} = 5 \times 10^{-16}$ erg cm^2 s^{-1}. For the remainder of the paper DOGs that are dominated by star formation following the SED-fitting decomposition procedure (i.e., labeled "host" in Table 2) will be named SF-DOGs, while the DOGs with a 20% contribution to the IR 8–1000 μm luminosity, derived according to the SED-fitting decomposition procedure (i.e., labeled "AGN" in Table 2), will be referred to as far-IR AGN DOGs.

We decompose the far-IR SED of the 22 X-ray detected DOGs into AGN and host galaxy components following the procedure described in Riguccini et al. (2015). Among these 22 X-ray DOGs, 9 of them have been included in Riguccini et al. (2015); however, taking advantage of the recent availability of spectroscopic redshifts for 22 of these we reanalyzed the SEDs of these sources. In the case of source DOG11 the reanalysis allowed for a satisfactory SED decomposition (in contrast with Riguccini et al. 2015), enabling us to classify it as dominated by a host galaxy component.

We find that only 7 out of the 22 X-ray detected DOGs are classified as AGNs based on their far-IR SED, i.e., AGN fraction >20%, see Riguccini et al. (2015). With the exception of one source that could not be properly decomposed using this procedure most likely due to a wrong redshift, the remaining X-ray detected DOGs (two-thirds of the sample) are all classified as dominated by a host galaxy SED component.

A summary of the AGN selections and the overlap between the different AGN criteria can be found on the Venn diagram presented on Figure 2. The numbers are expressed with respect to the total number of AGN candidates among the *Herschel* DOG population, i.e., the AGN candidates selected from a hard

Table 2
Herschel-DOGs with an X-ray Detection in the *Chandra* COSMOS Legacy Survey

DOG ID	X-ray ID	SED-fitting Flag	R.A.	Decl.	Redshift	HR	$N_{\rm H}$ $\times 10^{22}$ cm^{-2}	$L_{\rm ir}$ ($L_{\odot}$)
9	lid 3606	host	149.932	1.626	1.42	$0.75^{+0.25}_{-0.07}$	58.4–927	7.2×10^{11}
11	lid 2467	host	149.952	1.744	1.63	$-0.36^{+0.40}_{-0.29}$	0.01–12.7	2.0×10^{12}
42	lid 4354	host	149.478	2.133	1.58	$0.12^{+0.46}_{-0.32}$	4.46–36.3	9.8×10^{11}
56	lid 2346	host	149.733	2.335	1.58	$-0.90^{+0.005}_{-0.11}$	0.0–0.0	1.1×10^{12}
60	lid 3101	host	150.507	2.598	1.27	$0.86^{+0.14}_{-0.04}$	39.9–927	6.9×10^{11}
73	lid 319	AGN	150.426	2.725	1.20	$-0.04^{+0.09}_{-0.09}$	5.39–8.69	5.0×10^{11}
74	lid 3055	AGN	150.021	2.775	2.09	$0.62^{+0.38}_{-0.08}$	30.0–927	7.3×10^{11}
80	lid 3931	AGN	149.562	2.696	1.89	$0.65^{+0.26}_{-0.15}$	36.3–103	1.1×10^{12}
81	lid 1806	host	149.682	2.652	2.34	$-0.13^{+0.23}_{-0.21}$	2.29–20.5	1.5×10^{12}
95	lid 306	host	150.379	2.735	0.92	$0.06^{+0.09}_{-0.09}$	3.35–4.90	4.2×10^{11}
96	cid 201	AGN	149.906	1.917	1.49	$-0.25^{+0.08}_{-0.09}$	1.07–3.35	6.7×10^{11}
97	cid 817	host	150.063	1.945	2.15	$-0.19^{+0.33}_{-0.29}$	0.01–20.5	1.7×10^{12}
98	cid 1467	host	149.837	1.972	1.02	$-0.02^{+0.38}_{-0.33}$	0.55–8.69	6.5×10^{11}
99	lid 2663	···	149.779	1.586	1.24	$0.08^{+0.45}_{-0.31}$	2.08–16.9	−99
100	cid 1091	host	150.106	2.014	1.88	$-0.16^{+0.35}_{-0.24}$	0.34–16.9	2.8×10^{12}
101	lid 1646	AGN	150.787	2.151	1.47	$-0.17^{+0.02}_{-0.02}$	3.35–3.68	3.7×10^{11}
102	lid 1565	AGN	150.547	1.619	1.59	$-0.30^{+0.05}_{-0.06}$	0.88–2.52	6.5×10^{11}
103	lid 3587	AGN	149.931	1.735	1.43	$0.77^{+0.15}_{-0.12}$	30.0–64.3	9.4×10^{11}
104	cid 476	host	150.475	2.094	0.56	$0.21^{+0.04}_{-0.04}$	3.35–3.35	6.0×10^{11}
105	cid 593	host	150.472	2.324	0.89	$0.64^{+0.13}_{-0.12}$	11.6–16.9	3.3×10^{11}
106	cid 92	host	150.288	2.382	1.58	$-0.50^{+0.25}_{-0.24}$	0.01–2.52	2.9×10^{12}
107	cid 1917	host	149.998	2.578	2.42	$0.03^{+0.97}_{-0.07}$	24.8–927	4.3×10^{12}

Note. *SED-fitting flag* is based on far-IR SED decomposition (see Riguccini et al. 2015 for details).

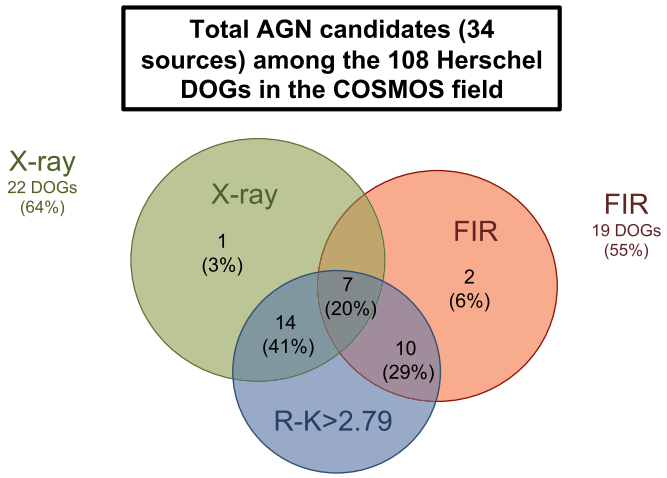

Figure 2. Venn diagram showing the distribution of AGN selections within the DOG population detected with *Herschel* in the COSMOS field: X-ray selected AGN DOGs in green, FIR selected AGN DOGs (based on SED-fitting) in red and $R - K$ cut in blue. The numbers and percentages are given with respect to the whole AGN population considered in this work (i.e., X-ray + FIR).

X-ray detection and from the SED-fitting decomposition using FIR data.

3.2. X-Ray Properties

The X-ray properties of the 22 DOGs individually detected by *Chandra* are described in Table 2. Given the faint X-ray fluxes, which yield a relatively low number of counts, detailed fitting to the observed X-ray spectrum is not possible for the majority of these sources. However, we can estimate the neutral hydrogen column density along the line of sight ($N_{\rm H}$) from the observed X-ray count rate, following the procedure described by Treister et al. (2009a). Briefly, this is done by assuming that the intrinsic spectrum is a power law with spectral index $\Gamma = 1.9$—in agreement with the observed average AGN spectrum (e.g., Nandra & Pounds 1994)—and computing the expected hardness ratio (HR). In the case of *Chandra*, the observed HR is defined as $(H - S)/(H+S)$, with S defined as the count rate in the soft X-ray band (0.5–2 keV) and H as the count rate in the hard band (2–8 keV). The expected HR is computed for each source individually considering the redshift of the source and a range in photoelectric absorption parameterized by the $N_{\rm H}$ value. The corresponding $N_{\rm H}$ value is then obtained by comparing the observed HR with the predicted ones. For mildly obscured sources, this is the same procedure followed by Marchesi et al. (2016) when there are fewer than 30 counts detected. For heavily obscured and CT sources, the observed X-ray spectrum can be more complicated than the simple power law and photoelectric absorption assumed before (e.g., Matt et al. 2000; Arévalo et al. 2014; Bauer et al. 2015). Hence, we further consider the predicted $N_{\rm H}$-HR relations using the physically motivated X-ray spectral libraries from Murphy & Yaqoob (2009), the so-called MYTorus models, which were not considered by Marchesi et al. (2016). The hence-derived $N_{\rm H}$ values are presented in Table 2 and Figure 3.

As can be seen, there are no major differences between the simple obscured power law and the MYTorus models for moderately obscured sources, $N_{\rm H} < 10^{23}$ cm^{-2}, up to $z \sim 2$, where most of our sources are located. However, as is expected, MYTorus predict in general lower HR values (softer X-ray spectra) for CT sources. This implies that just using the HR it is hard to discriminate a heavily obscured

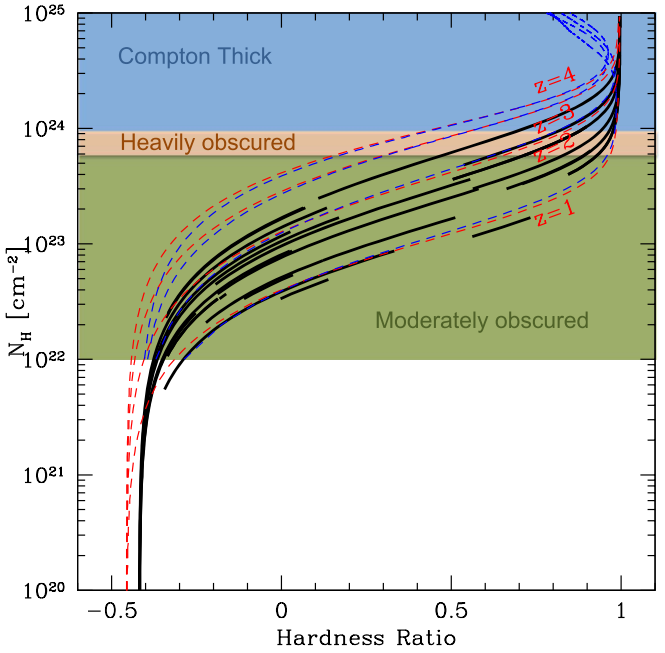

Figure 3. Neutral hydrogen column density (N_H) as a function of hardness ratio (HR) for the X-ray detected DOGs. The blue region (with $N_H > 10^{24}$ cm^{-2}) represents the Compton-thick (CT) population, while the orange one shows the location of heavily obscured sources with $N_H \sim 5 \times 10^{23}$ cm^{-2} and the green region situated right below corresponds to the moderately obscured sources, with N_H(cm^{-2}) $> 10^{22}$. The dashed lines show the expected relation between N_H and HR for sources at $z = 1$, 2, 3, and 4 assuming an intrinsic power law plus photoelectric absorption (red lines) and the MYTorus models (blue lines). The black solid segments show the location for the sources in Table 2 considering the observed HR and their uncertainties and assuming the simple power-law model.

$N_H > 5 \times 10^{23}$ cm^{-2} from a CT, $N_H > 10^{24}$ cm^{-2}, source. However, given the low number of counts detected for the X-ray sources in our sample, this procedure is the best we can do to attempt to identify CT AGNs.

According to the X-ray classification based on the derived N_H values, 6 out of the 22 X-ray detected DOGs (i.e., 27%) are plausible CT AGNs, namely DOG# 9, 60, 74, 80, 103, and 107. This is strictly an estimate, since as shown in Figure 3, sources with an HR in the ∼0.6–0.8 range can either be moderately/heavily obscured at $N_H \sim$ few $\times 10^{23}$ cm^{-2} or CT. Further, using this classification scheme, 15 are considered as moderately obscured AGNs, while only one of the X-ray detected DOGs has a low HR (DOG 56) consistent with being unobscured. The fraction of CT AGNs that we find in our sample is in good agreement with previous reports. For example, Georgakakis et al. (2010) found that the X-ray spectral properties of a sample of "low-redshift DOGs analogs" are consistent with moderate levels of obscuration and found in their sample a similar fraction of moderately obscured AGNs as in our work. Ricci et al. (2015) found that 27% ± 4% of their sample of 834 AGNs selected from the 70 month *Swift*/BAT catalog in the local universe corresponds to CT AGNs. This is somewhat larger than the value predicted by Aird et al. (2015) at low redshifts but still in good agreement with the report by Burlon et al. (2011) using a smaller sample of 200 AGNs. It would have been reasonable to expect that DOGs should have a higher fraction of CT sources because by definition they have dustier host galaxies. However, these results, combined with the evidence presented in Section 4.4 appear to indicate that there is no significant difference with the general AGN population. Thus, we can speculate that the obscuration, at least in the most extreme cases has to be nuclear and roughly independent of the properties of the host galaxy, as also concluded by Ricci et al. (2017) for a hard X-ray selected AGN sample and using statistical arguments by Buchner & Bauer (2017).

3.3. X-Ray Stacking

Previous studies have shown that stacking in the X-ray is a powerful technique that allows the detection of emission from objects lying below the formal detection limit for individual sources (e.g., Brandt et al. 2001). Chandra is particularly well suited for this thanks to its very low and stable background. We perform X-ray stacking for the DOGs in the area covered by the COSMOS *Chandra* Legacy data using the web-based CSTACK code[23] developed by Takamitsu Miyaji. Stacking was performed in two bands independently: soft (0.5–2 keV) and hard (2–5 keV). Chandra internal background being dominated by strong emission lines above 7 keV, we limit the high energy band threshold to 5 keV to limit the internal background. Prior to stacking, we removed all the sources that were individually detected by *Chandra*; this reduced our sample from 108 far-IR detected DOGs to 86. After removing DOGs that are too close to an X-ray source, the stacking with CSTACK was performed on 76 objects. The radius of the exclusion region varies with the off axis angle, corresponding to the 90% encircled counts fraction radii, with a minimum of 1.0 arcsec and a maximum of 7.0 arcsec. We obtain a mean count rate on the soft band of $8.56 \pm 1.89 \times 10^{-6}$ cts s^{-1}. In contrast, no significant detection is obtained in the hard band using a $\sim 3\sigma$ threshold. We provide for different stacking approaches an estimate for the flux only when the detection is above 3σ (see Table 3).

In order to convert count rates into fluxes we use the Portable, Interactive Multi-Mission Simulator (PIMMS) tool for the *Chandra* Observatory.[24] Assuming the corresponding *Chandra*-Cycle 14/ACIS response functions, an intrinsic power-law spectrum with $\Gamma = 1.9$, a Galactic absorption value of 2.6×10^{20} cm^{-2} (Willingale et al. 2013), and a representative intrinsic absorption of 10^{23} cm^{-2} at $z = 2$ (median redshift of our sample of X-ray undetected DOGs), we find a conversion factor from counts-per-second to flux of 5.2×10^{-12} erg cm^{-2} s^{-1}/(cts s^{-1}) in the soft band. We find that the average observed X-ray flux for the X-ray undetected DOGs is $S_{0.5-2\,\mathrm{keV}} = 4.4 \times 10^{-17}$ erg cm^{-2} s^{-1} in the soft band, a factor of 10 lower than the average value for the X-ray detected DOGs. The stacked signal in the hard band is below a 3σ detection (cf. Table 3).

4. Discussion

4.1. X-Ray Stacking of Specific Population Subsamples

In this section, we study the possible dependence of our X-ray stacking results on other parameters of the DOGs such as AGN activity, star formation, redshift, and 24 μm flux. Our results are described in this section and summarized in Table 3.

[23] http://cstack.ucsd.edu/ or http://lambic.astrosen.unam.mx/cstack/
[24] http://cxc.harvard.edu/toolkit/pimms.jsp

Table 3
Characteristics of the Different Subsamples of *Herschel*-DOGs from Riguccini et al. (2015) on Which X-Ray Stacking Has Been Performed with the C-STACK Procedure

Subsample	Number of Sources Used for stacking	Number of FIR-AGN DOGs used for stacking	Median Count Rate Soft band (1e−06)	Flux[a] Soft Band (erg s^{-1} cm^{-2}) (1e−17)	Median Count Rate 2–5 keV (1e−06)	Flux[a] Hard Band (2–8 keV) (erg s^{-1} cm^{-2}) (1e−17)
All Undetected	76	10	8.56 ± 1.89	4.43	6.01 ± 2.24	···
SF Undetected	59	0	7.39 ± 2.05	3.82	6.52 ± 2.55	···
AGN Undetected	10	10	10.5 ± 6.45	···	4.24 ± 6.43	···
$R - K > 2.79$	69	10	8.94 ± 2.02	4.62	7.24 ± 2.41	1.76
SFR > 200	55	6	8.83 ± 2.18	4.57	5.03 ± 2.63	···
SFR > 300	38	5	10.1 ± 2.86	5.65	4.72 ± 3.16	···
SFR > 400	23	4	5.63 ± 3.40	···	1.94 ± 3.86	···
$z < 1.9$	28	0	9.53 ± 3.01	4.94	7.18 ± 3.91	···
$1.9 < z < 2.3$	24	2	10.5 ± 3.42	5.43	8.70 ± 4.17	···
$2.3 < z < 3$	25	8	7.57 ± 3.41	···	7.22 ± 3.63	···
0.09 < F24 < 0.36	30	1	7.14 ± 2.77	···	7.20 ± 3.56	···
0.36 < F24 < 0.60	26	1	5.58 ± 3.27	···	4.08 ± 3.76	···
0.60 < F24 < 4.74	21	8	15.6 ± 4.19	8.08	3.81 ± 4.45	···

Note.
[a] Fluxes are computed using PIMMS only when a detection $>3\sigma$ significant is achieved.

4.1.1. Effect of AGN Activity on X-Ray Stacking

Following the far-IR classification of Riguccini et al. (2015), we stacked the subsample of "star-forming" DOGs (those dominated by a host SED component) and that of far-IR AGN DOGs. Out of the DOGs that are not detected in the X-rays, a total of 66 are classified as "host" DOGs by Riguccini et al. (2015) and 12 are classified as AGNs; note that only 10 sources of the latter were used to perform the stacking after eliminating two due to proximity to an X-ray source. The stacked signal in the soft band for the "host" DOGs is reported in Table 3. Most likely due to the low number of sources, no signal was detected either in the soft nor the hard band of the AGN far-IR DOGs.

Fiore et al. (2008, 2009) and Treister et al. (2009a) showed that imposing a color cut of $R - K > 2.79$ on a DOG sample increases the probability of selecting AGN DOGs. It is worth noting that we find similar results with our X-ray stacking analysis. Indeed the only subsample where we obtained a stacked emission in the hard band (i.e., with detection $>3\sigma$) is for the DOG population with $R - K > 2.79$, underlying a higher AGN activity in this subsample. Based on this result, we estimate the HR of the stacked signal for the $R - K$ cut sample and obtain a value of 0.02 ± 0.29. Considering this result and the redshifts of the sources that went into the stacking, we can see from Figure 3 that this contribution is likely associated with moderately obscured AGN activity.

4.1.2. Effect of Redshift and Star Formation Activity on X-Ray Stacking

In order to gauge the impact that redshift may have on our results, we divide our sample of 86 X-ray undetected DOGs roughly evenly into three redshift bins and perform X-ray stacking independently on these three subsamples: 30 sources at $z < 1.9$, 27 sources with $1.9 < z < 2.3$ and 29 sources with $2.3 < z < 3$. After excluding DOGs that are too close to an X-ray source the stacking was performed on 28 sources at $z < 1.9$, 24 at $1.9 < z < 2.3$ and 25 at $2.3 < z < 3$, with corresponding median redshifts of $\langle z \rangle \sim 1.75$, 2.0 and 2.7, respectively. Table 3 displays our findings, where quoted fluxes are calculated assuming a conversion factor of 5.18×10^{-12} erg cm^{-2} s^{-1}/(cts s^{-1}). The X-ray stacking procedure yielded significant detections (i.e., $>3\sigma$) in the soft band for the two lower redshift bins, but not for the higher redshift bin probed in this study. We found no significant detections in the hard band for any of the redshift bins. Based on these results we do not find any evidence for a significant redshift evolution in the average soft X-ray flux of the sample.

We consider three bins of increasingly intense star formation activity—SFR $> 200\,M_{\odot}\,\mathrm{yr}^{-1}$ (55 sources), SFR $> 300\,M_{\odot}\,\mathrm{yr}^{-1}$ (38 sources) and SFR $> 400\,M_{\odot}\,\mathrm{yr}^{-1}$ (23 sources)—neither of which present a signal in the hard band. We merely find a detection in the soft band for the bins with sources displaying SFR $> 200\,M_{\odot}\,\mathrm{yr}^{-1}$ and SFR $> 300\,M_{\odot}\,\mathrm{yr}^{-1}$. Based on these results we are unable to probe for any trends with respect to star formation activity.

4.1.3. Effect of 24 μm Flux on X-Ray Stacking

To analyze the effect of the 24 μm flux on the X-ray properties of the DOGs, we split our sample into three 24 μm flux bins: $0.09 < \mathrm{F24}(\mu\mathrm{Jy}) < 0.36$, $0.36 < \mathrm{F24}(\mu\mathrm{Jy}) < 0.60$, $0.60 < \mathrm{F24}(\mu\mathrm{Jy}) < 4.74$ with mean redshifts of $\langle z \rangle \sim 2.1$, 2.1 and 2.2 respectively. We performed X-ray stacking on these three subsamples independently and only find a $> 3\sigma$ detection for the brightest 24 μm in the soft band. However, based on tentative detections ($<3\sigma$) for the fainter 24 μm bins, the soft band stacking results suggest a dependence on the 24 μm flux, with higher X-ray fluxes associated with brighter 24 μm sources. This is an expected trend, as earlier works (e.g., Treister et al. 2006; Riguccini et al. 2015) have shown that the AGN fraction increases strongly with 8 μm luminosity and hence with the 24 μm flux as well.

4.2. AGN Fraction

We show in Figure 4 the fraction of far-IR detected DOGs that are classified as AGNs as a function of the 24 μm flux,

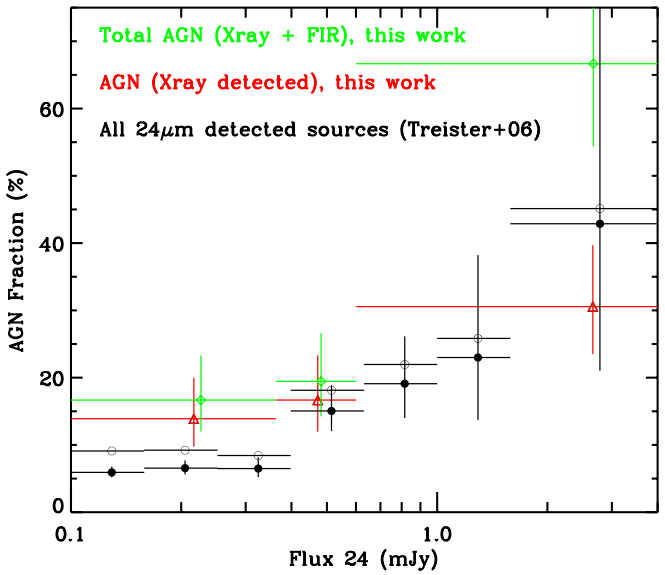

Figure 4. Fraction of *Herschel*-DOGs classified as AGNs as a function of 24 μm flux. The green diamonds show the combination of far-IR and X-ray selected AGNs, while the red triangles show only the X-ray selected AGNs. The horizontal error bars show the size of the flux bins, while vertical error bars show the 1σ Poissonian errors on the number of sources. As a comparison we show the fraction of sources classified as AGNs in the GOODS field (filled black circles) and the fraction corrected by the AGNs expected to be missed by X-ray selection, as estimated using an AGN population synthesis model (open black circles), as described by Treister et al. (2006).

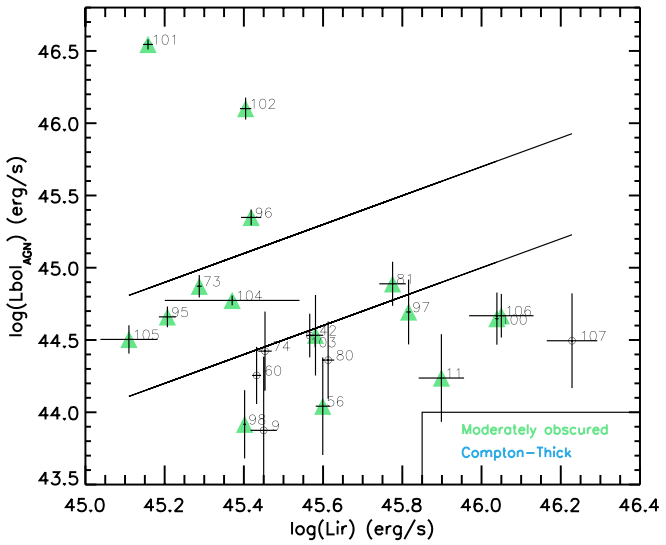

Figure 5. AGN bolometric luminosity as a function of the infrared luminosity for the 21 X-ray detected DOGs (CT candidates: blue stars; moderately obscured AGNs: green triangles) with an FIR SED-decomposition fit that led to the determination of the IR luminosity. Error bars in luminosities are obtained directly from the errors in the fluxes, accounting for the observed spread in bolometric correction in X-rays. The numbers next to the symbols correspond to the DOG ID # from Riguccini et al. (2015), also listed in Table 2. The lower and upper solid lines represent 10% and 50% of the infrared luminosity, respectively.

considering only X-ray classification (red triangles) and the combined X-ray and far-IR SED-based classification (green diamonds). We can see that the AGN fraction increases rapidly toward higher 24 μm fluxes, particularly when considering the combined far-IR and X-ray detected analysis. Brand et al. (2006) found that at the brightest 24 μm fluxes, 74% $\pm$ 21% of their sample of LIRGs with $z > 0.6$ have their mid-IR emission dominated by an AGN. Compared to the entire 24 μm population in the GOODS field (see also, e.g., Treister et al. 2006), we only see a significant difference between the DOGs and the wider 24 μm population at the lowest 24 μm fluxes. However, the X-ray-based AGN fraction shown in Figure 4 is strictly based on considering merely those AGN DOGs with individual X-ray detections. In the light of our X-ray stacking results, we note that AGN activity is not limited to this sample of individually X-ray detected DOGs, but that a mix nature (AGN and star formation) exists within the population of the individually X-ray undetected DOGs. In an effort to constrain the contribution to the AGN fraction from the X-ray undetected population, we compared our stacked point with results from X-ray normal galaxies from Lehmer et al. (2016) and with our X-ray detected DOGs and found a contribution of 20% from AGN activity for the stacked sample. Considering that the X-ray undetected DOG sample in question is comprised of 76 DOGs, this translates into a potential increase of the AGN fraction by 15 significantly obscured DOGs.

Our stacking analysis showed that X-ray fluxes increase with 24 μm flux. This is consistent with the observed trend within the X-ray detected DOG population, with an observed increase of the total AGN fraction in the brightest 24 μm bins (see Figure 4), as previously reported by, e.g., Dey et al. (2008) and Fiore et al. (2009). Taking into account the potential nonnegligible fraction of highly obscured AGNs missed even with our (X-ray+far-IR) combined analysis but revealed within our undetected DOG sample, we expect that the AGN fraction traced by the DOG population may be even higher within the brightest 24 μm bins. Combined with the observed difference in AGN fraction at the faintest 24 μm bins between the DOG population and the GOODS 24 μm population as a whole from Treister et al. (2006), these results point to the DOG population as an effective means of selecting AGNs, particularly so in the case of high obscuration.

4.3. Star Formation Rates

In order to identify a potential AGN contribution to the IR luminosity used to infer star formation rates, we first derive the AGN bolometric luminosity for the 22 X-ray detected DOGs (0.5–10 keV), estimating it from the intrinsic (i.e., absorption-corrected) X-ray luminosity and assuming a fixed factor of 10 for the bolometric correction, as reported by, e.g., Rigby et al. (2009) and Vasudevan & Fabian (2009). While a luminosity dependence of the bolometric correction has been claimed in the past (e.g., Marconi et al. 2004), more recent work (Lusso et al. 2012) shows that in the luminosity range spanned by our sample the expected changes in luminosity are relatively small, a factor of $\sim$2, and consistent with the observed dispersion, as can be seen in Figure 8 of Lusso et al. (2012), thus justifying our conservative choice of a constant bolometric correction. We then conclude that in most cases the AGN accounts for less than 50% of the IR luminosity, as can be seen in Figure 5 for the 21 X-ray detected DOGs with an FIR-fit. This conclusion holds even considering a bolometric correction that is $\sim$2$\times$ higher for the most luminous sources. Hence, even in sources that contain an AGN, the nuclear emission does not make a significant contribution to the IR luminosity, which is most likely due to processes related to the star formation activity. In particular, we find that $\sim$60% of all moderately obscured AGNs and all CT candidates display a $\leqslant$10% AGN contribution to the IR luminosity.

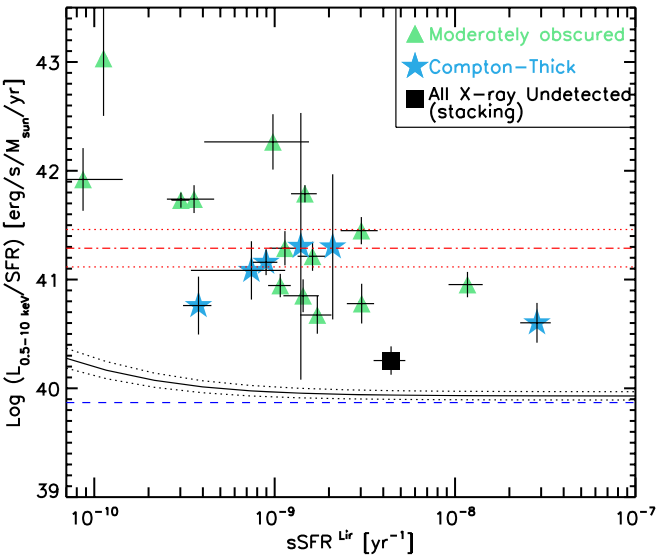

Figure 6. Logarithm of the X-ray luminosity (0.5–10 keV) per unit SFR vs. sSFR for the 21 X-ray detected DOGs (CT candidates: blue stars; moderately obscured AGNs: green triangles) with FIR SED-decomposition fit. The black solid curve represents the best-fit solution from the results of Lehmer et al. (2016) for 116 X-ray detected normal galaxies and the two dotted lines show the error bars on this fit. The blue dashed line shows the results from Mineo et al. (2014) for $z < 1.3$ X-ray and radio detected galaxies. The red dotted–dashed line is the median value for the X-ray detected sources and we are showing the median error bars with the two red dotted lines. The black rectangle shows the logarithm of the X-ray luminosity (0.5–10 keV) per unit SFR vs. sSFR for the X-ray undetected sample (see Section 3.3).

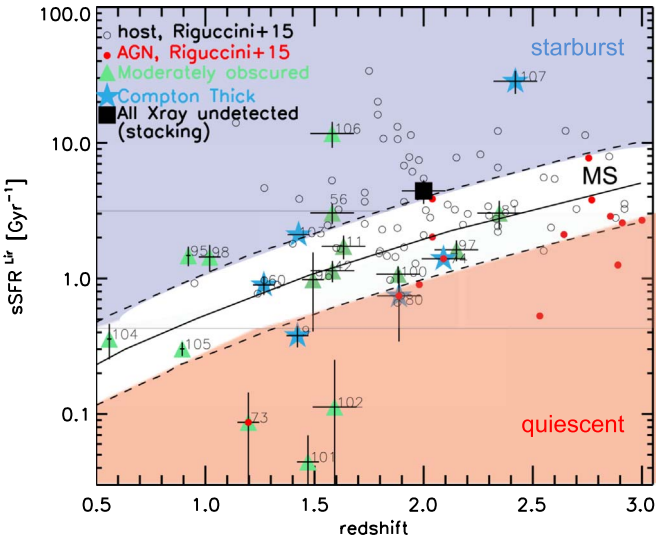

Figure 7. Redshift evolution of the specific SFR (sSFR = SFR/M_*) detected in the infrared (black and red circles) and in X-rays (CT candidates: blue stars; heavily obscured AGNs: green triangles). The SFR rate is calculated from the infrared luminosity obtained from the SED-fitting procedure described by Riguccini et al. (2015), i.e., removing the AGN contribution. The solid line represents the star-forming main sequence from Elbaz et al. (2011), while the dashed lines are a factor 2 above and below this fit. Most of the CT AGN (blue stars) are within the MS. The upper part of the plot corresponds to the starburst regime while the lower part corresponds to the quiescent phase. The black rectangle shows the location of the X-ray undetected DOG population (i.e., the stacking analysis, see Section 3.3 for details) with respect to the MS.

Figure 6 displays the X-ray luminosity per unit of star formation rate, in units of erg $s^{-1}/(M_\odot\,yr^{-1})$, as a function of the specific SFR (sSFR) for the 21 X-ray detected sources with FIR SED-decomposition fit. The stellar masses are taken from SED-fitting analyses using 30 bands in COSMOS from Ilbert et al. (2009). The SFR is obtained using the Kennicutt (1998) relation with IR luminosity. We use the IR luminosity obtained in this work with SED-fitting taking into account the contribution of an AGN component to the host galaxy. We are confident in our stellar masses and SFR estimates because they are in very good agreement with the recent work of Suh et al. (2017) on Type 2 AGN host galaxies in the *Chandra* COSMOS Legacy Survey. Our stellar masses (median log $M_* = 11.26 \pm 0.07$) agree within the error bars with their value (median log $M_{*,\mathrm{Suh}} = 11.00 \pm 0.20$) and our median SFR ($131 \pm 39\,M_\odot\,yr^{-1}$) agrees with their median value as well ($173^{+45}_{-12}\,M_\odot\,yr^{-1}$). The black dotted lines in Figure 6 delimit the area populated by normal galaxies from Lehmer et al. (2016, orange area). The fact that all of the sources in our sample are above the line found for normal (i.e., non-AGN) galaxies, as reported by Mineo et al. (2014), in most cases by more than an order of magnitude indicates that the X-ray emission is most likely dominated by the AGN emission, even if the IR is not.

We further include in Figure 6 the results of our stacking analysis for all X-ray undetected DOGs. In order to do this, we used the PIMMS tool to convert the flux of the X-ray undetected DOGs stacked sample from Table 3 into the extrapolated 5–10 keV X-ray luminosity with a median redshift of $z = 2$. The stacked sample has a median sSFR of $4.42 \pm 0.88 \times 10^{-9}\,(yr^{-1})$. We are quantifying the AGN contribution to the X-ray undetected DOG population using the stacked point in this figure. If the stacked sample was only star formation activity, it would be located on the black solid curve with log $(Lx/\mathrm{SFR}) = 39.93\,(\mathrm{erg\,s^{-1}}/M_\odot\,yr^{-1})$ at the median sSFR of the X-ray undetected sample. If it was only coming from AGN activity (i.e., 100% contribution) it would be located on the red dashed–dotted line (i.e., log $(Lx/\mathrm{SFR}) = 41.28\,(\mathrm{erg\,s^{-1}}/M_\odot\,yr^{-1})$). We then estimate the AGN contribution of the stacked sample at ∼20%. We note here that we found a similar AGN contribution using the $R - K > 2.79$ X-ray undetected DOGs sample.

4.4. Specific Star Formation Rate of the DOG Population: Where Do the AGN DOGs Lie with Respect to the Main Sequence (MS)?

Recent studies have pointed to the existence of a so-called "MS" of star-forming galaxies up to $z \sim 2.5$ where galaxies undergoing star formation activity typically lie within a well-defined region in the SFR-stellar mass diagram (e.g., Daddi et al. 2007; Elbaz et al. 2011; Whitaker et al. 2012; Genzel et al. 2015; Tacconi et al. 2018). Riguccini et al. (2015) showed, based on the MS definition of Elbaz et al. (2011), that far-IR AGN DOGs mainly lie on or below the MS, while DOGs dominated by a host component lie on the MS and above it, within the starburst regime. These results underline the diversity found in the DOG population. Taking advantage of the *Herschel* data, we can derive, using SED-fitting at far-IR wavelengths, reliable IR luminosities and hence star formation rates, and potential AGN contributions in the IR for the DOGs in our sample.

Figure 7 shows the evolution of the specific SFR (sSFR) of DOGs with cosmic time. The AGN DOGs (both X-ray and far-IR) appear to present a lower sSFR than SF-DOGs. We run a KS test to verify how distinct the distributions in sSFRs are and find a low probability of 1.6×10^{-4} that they arise from the

same parent distribution. The majority of the AGNs-DOGs (both far-IR and X-ray) populate the area around and below the MS, with only two sources lying well above it: one CT candidate and a moderately obscured AGN.

We do not see clear differences in behavior between the CT candidates and the moderately obscured AGNs in Figure 7. According to the evolutionary scenario of Treister et al. (2010), the highly obscured CT AGNs correspond to the early, very dust-enshrouded, SMBH growth phase in a major galaxy merger; moderately obscured AGNs correspond in turn to a later stage in this evolutionary scenario, when the energetic feedback related to the SMBH accretion have already started heating up the dust and gas of the galaxy, shutting down star formation activity. In this picture, we expect the CT candidates to lie slightly above the moderately obscured AGNs in the sSFR-redshift diagram, which does not appear to be the case. This surprising result that CT AGNs are not preferentially found above the MS has been found as well in spectroscopically selected CT sample (e.g., Georgantopoulos et al. 2013; Lanzuisi et al. 2015). Hence, this further confirms the scenario presented in Section 3.2, suggesting that at least for the most extreme sources, the obscuration has to be nuclear and thus not directly connected to the evolutionary stage of the host galaxy.

We note that the large uncertainties on the $N_{\rm H}$ determinations make it hard to discriminate between CT and moderately obscured AGNs. This in turn also affects the derivation of the AGN contribution and has an impact in $L_{\rm IR}$ and SFR estimates. This could potentially explain the lack of an observed difference of behavior between the two populations of X-ray detected AGNs. However, we have to consider the detectability of those sources. Assuming that the far-IR AGNs have the same X-ray luminosity as the X-ray detected ones but they are lying at higher redshifts and hence have lower fluxes, we run C-stack on 19 random undetected DOGs to check if those far-IR AGN DOGs would have been detected by X-ray stacking, finding no significant detection.

5. Conclusions

Searching for obscured AGNs is of main importance because AGN synthesis models for the Cosmic X-ray background (CXRB) predict a large number of obscured AGNs including CT AGNs. However, even the deepest *Chandra* and *XMM-Newton* surveys were able to detect only a few of them until now. Our study combines exquisite new *Chandra* data with far-infrared *Herschel* data to catch obscured AGNs at $z \sim 2$. In this work we aimed to characterize the X-ray properties of the DOG ($F_{24\ \mu{\rm m}}/F_R > 1000$) population with far-IR detections by the *Herschel* Space Telescope. Our sample is composed of 108 DOGs in the COSMOS field and we relied on the *Chandra* COSMOS Legacy Survey X-ray and on the *Herschel* Observatory data to undertake our analysis.

Out of 108 DOGs, 22 (i.e., 20% of the sample) are individually detected in the X-ray soft and hard bands thanks to the increased coverage in area and sensitivity of the *Chandra* COSMOS Legacy Survey observations. Based on our estimates of the corresponding neutral hydrogen column density along the line of sight ($N_{\rm H}$), we find that 6 of these X-ray detected DOGs (i.e., 27%) are CT candidates, 15 (68%) are moderately obscured AGNs and one is consistent with being unobscured. Our results are in excellent agreement with previous reports (i.e., Ricci et al. 2015) that found a fraction of CT AGNs of $27\% \pm 4\%$. This suggests that the fraction of CT sources is not different from that of the general AGN population and hence the obscuration, at least in the most extreme cases, appears to be independent of the amount of dust in the host and hence is most likely nuclear.

We study the SED of the 22 X-ray detected DOGs, based on (rest-frame) optical-through-IR data, and find that only 7 are classified as AGNs following the SED-fitting method described in Riguccini et al. (2015). We note that out of the 19 far-IR AGN DOGs identified by Riguccini et al. (2015), these 7 are the only ones with *Chandra* X-ray detection. This clearly shows how using far-IR to select obscured AGNs is crucial to complement an X-ray analysis, allowing us to probe a wider range of AGNs.

Our main results are the following:

1. We find that the X-ray detected AGN DOGs and the far-IR AGN DOGs typically display similar near-IR and mid-to-far-IR colors. Both populations are also typically found on the MS of star-forming galaxies or below it. The main difference these populations appear to display is in their redshift distributions, with the far-IR AGN DOGs being typically found at larger distances. Together, these results suggest that the two populations share most of their physical properties and that the lack of detection in the X-ray band for the bulk of far-IR AGN DOGs is explained by the difference in redshift distributions. This strongly underlines the critical need of multiwavelength studies in order to obtain a more complete census of the obscured AGN population out to higher redshifts.
2. Based on earlier findings by Fiore et al. (2008, 2009) and Treister et al. (2009a), who showed that a color cut of $R - K > 2.79$ on a DOG sample increases the probability of selecting AGNs, we stacked all individually undetected DOGs above this color cut. This resulted in the strongest stacked signal from our subsample stacking, pointing to a higher AGN fraction, likely associated with moderately obscured AGN activity.
3. We demonstrate that the combined population of X-ray detected and far-IR DOGs is effective at selecting AGNs, compared to the 24 μm population as a whole (as done within the GOODs field by, e.g., Treister et al. 2006). Moreover, X-ray stacking of individually undetected DOGs points to a mix between AGN activity and star formation. We want to stress here how much our AGN far-IR *Herschel* SED-based classification is important. Indeed, if only considering X-ray detections, DOGs would have the same AGN fraction or even lower than a 24 μm selected population. This shows the critical need of deep far-IR surveys to probe AGN activity in star-forming galaxy samples.

This work emphasizes the important role that the DOG population, in particular, the combined X-ray and far-IR detected DOG population, plays in the effort to get a more complete census of the AGN population at high redshift, particularly for the highly obscured population.

We would like to thank the anonymous referee for very useful comments that significantly improved the paper. COSMOS is based on observations with the NASA/ESA *Hubble Space Telescope*, obtained at the Space Telescope Science Institute, which is operated by AURA, Inc., under

NASA contract NAS 5-26555; also based on data collected at the Subaru Telescope, which is operated by the National Astronomical Observatory of Japan; *XMM-Newton*, an ESA science mission with instruments and contributions directly funded by ESA Member States and NASA; the European Southern Observatory, Chile; Kitt Peak National Observatory, Cerro Tololo Inter-American Observatory, and the National Optical Astronomy Observatory, which are operated by the Association of Universities for Research in Astronomy (AURA), Inc., under cooperative agreement with the National Science Foundation; the National Radio Astronomy Observatory, which is a facility of the National Science Foundation operated under cooperative agreement by Associated Universities, Inc; and the Canada–France–Hawaii Telescope, operated by the National Research Council of Canada, the Centre National de la Recherche Scientifique de France, and the University of Hawaii.

PACS has been developed by a consortium of institutes led by MPE (Germany) and including UVIE (Austria); KU Leuven, CSL, IMEC (Belgium); CEA, LAM (France); MPIA (Germany); INAF-IFSI/OAA/OAP/OAT, LENS, SISSA (Italy); IAC (Spain). This development has been supported by the funding agencies BMVIT (Austria), ESA-PRODEX (Belgium), CEA/CNES (France), DLR (Germany), ASI/INAF (Italy), and CICYT/MCYT (Spain).

SPIRE has been developed by a consortium of institutes led by Cardiff University (UK) and including University of Lethbridge (Canada), NAOC (China), CEA, LAM (France), IFSI, University of Padua (Italy), IAC (Spain), Stockholm Observatory (Sweden), Imperial College London, RAL, UCL-MSSL, UKATC, University of Sussex (UK), Caltech, JPL, NHSC, University of Colorado (USA). This development has been supported by national funding agencies: CSA (Canada); NAOC (China); CEA, CNES, CNRS (France); ASI (Italy); MCINN (Spain); SNSB (Sweden); STFC, UKSA (UK) and NASA (USA). SPIRE has been developed by a consortium of institutes led by Cardiff Univ. (UK) and including Univ. Lethbridge (Canada); NAOC (China); CEA, LAM (France); IFSI, Univ. Padua (Italy); IAC (Spain); Stockholm Observatory (Sweden); Imperial College London, RAL, UCL-MSSL, UKATC, Univ. Sussex (UK); Caltech, JPL, NHSC, Univ. Colorado (USA). This development has been supported by national funding agencies: CSA (Canada); NAOC (China); CEA, CNES, CNRS (France); ASI (Italy); MCINN (Spain); SNSB (Sweden); STFC, UKSA (UK); and NASA (USA).

E.T. acknowledges support from CONICYT-Chile grants Basal-CATA PFB-06/2007 and AFB-170002, FONDECYT Regular 1160999 and 1190818, and Anillo de ciencia y tecnología ACT1720033. K.M.D. and T.S.G. are thankful for the support of the Productivity in Research Grant of the Brazilian National Council for Scientific and Technological Development (CNPq). T.M. and the development of CSTACK are supported by CONACyT IB 252531 and UNAM-DGAPA PAPIIT IN104216 E.L. is supported by a European Union COFUND/Durham Junior Research Fellowship (under EU grant agreement No. 609412) G.L. acknowledges support from the FP7 Career Integration Grant "eEASy" (CIG 321913) and grant ASI/INAF I/037/12/0-011/13. C.R. acknowledge financial support from FONDECYT 1141218, Basal-CATA PFB–06/2007 and the China-CONICYT fund.

ORCID iDs

Ezequiel Treister https://orcid.org/0000-0001-7568-6412
Carolin Cardamone https://orcid.org/0000-0003-4608-6340
Guenther Hasinger https://orcid.org/0000-0002-0797-0646
Anton M. Koekemoer https://orcid.org/0000-0002-6610-2048
Giorgio Lanzuisi https://orcid.org/0000-0001-9094-0984
Elisabeta Lusso https://orcid.org/0000-0003-0083-1157
Dieter Lutz https://orcid.org/0000-0003-0291-9582
Stefano Marchesi https://orcid.org/0000-0001-5544-0749
Takamitsu Miyaji https://orcid.org/0000-0002-7562-485X
Francesca Pozzi https://orcid.org/0000-0002-7412-647X
Claudio Ricci https://orcid.org/0000-0001-5231-2645
Giulia Rodighiero https://orcid.org/0000-0002-9415-2296
Mara Salvato https://orcid.org/0000-0001-7116-9303
Dave Sanders https://orcid.org/0000-0002-1233-9998
Kevin Schawinski https://orcid.org/0000-0001-5464-0888
Hyewon Suh https://orcid.org/0000-0002-2536-1633

References

Aird, J., Coil, A. L., Georgakakis, A., et al. 2015, MNRAS, 451, 1892
Akylas, A., Georgakakis, A., Georgantopoulos, I., Brightman, M., & Nandra, K. 2012, A&A, 546, A98
Arévalo, P., Bauer, F. E., Puccetti, S., et al. 2014, ApJ, 791, 81
Ballantyne, D. R., Draper, A. R., Madsen, K. K., Rigby, J. R., & Treister, E. 2011, ApJ, 736, 56
Ballantyne, D. R., Everett, J. E., & Murray, N. 2006, ApJ, 639, 740
Baronchelli, L., Koss, M., Schawinski, K., et al. 2017, MNRAS, 471, 364
Bauer, F. E., Arévalo, P., Walton, D. J., et al. 2015, ApJ, 812, 116
Berta, S., Magnelli, B., Nordon, R., et al. 2011, A&A, 532, A49
Brand, K., Dey, A., Weedman, D., et al. 2006, ApJ, 644, 143
Brandt, W. N., Hornschemeier, A. E., Schneider, D. P., et al. 2001, ApJL, 558, L5
Brightman, M., Nandra, K., Salvato, M., et al. 2014, MNRAS, 443, 1999
Brusa, M., Civano, F., Comastri, A., et al. 2010, ApJ, 716, 348
Brusa, M., Zamorani, G., Comastri, A., et al. 2007, ApJs, 172, 353
Buchner, J., & Bauer, F. E. 2017, MNRAS, 465, 4348
Buchner, J., Georgakakis, A., Nandra, K., et al. 2015, ApJ, 802, 89
Burlon, D., Ajello, M., Greiner, J., et al. 2011, ApJ, 728, 58
Capak, P., Aussel, H., & Ajiki, M. 2007, ApJS, 172, 99
Civano, F., Hickox, R. C., Puccetti, S., et al. 2015, ApJ, 808, 185
Civano, F., Marchesi, S., Comastri, A., et al. 2016, ApJ, 819, 62
Comastri, A., Ranalli, P., Iwasawa, K., et al. 2011, A&A, 526, L9
Comastri, A., Setti, G., Zamorani, G., & Hasinger, G. 1995, A&A, 296, 1
Daddi, E., Dickinson, M., Morrison, G., et al. 2007, ApJ, 670, 156
Desai, V., Armus, L., Spoon, H. W. W., et al. 2007, ApJ, 669, 810
Dey, A., Soifer, B. T., Desai, V., et al. 2008, ApJ, 677, 943
Elbaz, D., Dickinson, M., Hwang, H. S., et al. 2011, A&A, 533, A119
Feruglio, C., Daddi, E., Fiore, F., et al. 2011, ApJL, 729, L4
Fiore, F., Grazian, A., Santini, P., et al. 2008, ApJ, 672, 94
Fiore, F., Puccetti, S., Brusa, M., et al. 2009, ApJ, 693, 447
Genzel, R., Lutz, D., Sturm, E., et al. 1998, ApJ, 498, 579
Genzel, R., Tacconi, L. J., Lutz, D., et al. 2015, ApJ, 800, 20
Georgakakis, A., Rowan-Robinson, M., Nandra, K., et al. 2010, MNRAS, 406, 420
Georgantopoulos, I., Comastri, A., Vignali, C., et al. 2013, A&A, 555, A43
Gilli, R., Comastri, A., & Hasinger, G. 2007, A&A, 463, 79
Gilli, R., Salvati, M., & Hasinger, G. 2001, A&A, 366, 407
Ilbert, O., Capak, P., Salvato, M., et al. 2009, ApJ, 690, 1236
Joseph, R. D. 1999, Ap&SS, 266, 321
Juneau, S., Dickinson, M., Alexander, D. M., & Salim, S. 2011, ApJ, 736, 104
Juneau, S., Dickinson, M., Bournaud, F., et al. 2013, ApJ, 764, 176
Kennicutt, R. C., Jr. 1998, ApJ, 498, 541
Lansbury, G. B., Stern, D., Aird, J., et al. 2017, ApJ, 836, 99
Lanzuisi, G., Ranalli, P., Georgantopoulos, I., et al. 2015, A&A, 573, A137
Le Floc'h, E., Aussel, H., Ilbert, O., et al. 2009, ApJ, 703, 222
Lehmer, B. D., Basu-Zych, A. R., Mineo, S., et al. 2016, ApJ, 825, 7
Lusso, E., Comastri, A., Simmons, B. D., et al. 2012, MNRAS, 425, 623
Lutz, D., Spoon, H. W. W., Rigopoulou, D., Moorwood, A. F. M., & Genzel, R. 1998, ApJL, 505, L103

Marchesi, S., Lanzuisi, G., Civano, F., et al. 2016, ApJ, 830, 100
Marconi, A., Risaliti, G., Gilli, R., et al. 2004, MNRAS, 351, 169
Matt, G., Fabian, A. C., Guainazzi, M., et al. 2000, MNRAS, 318, 173
Menéndez-Delmestre, K., Blain, A. W., Smail, I., et al. 2009, ApJ, 699, 667
Mineo, S., Gilfanov, M., Lehmer, B. D., Morrison, G. E., & Sunyaev, R. 2014, MNRAS, 437, 1698
Mullaney, J. R., Alexander, D. M., Goulding, A. D., & Hickox, R. C. 2011, MNRAS, 414, 1082
Mullaney, J. R., Del-Moro, A., Aird, J., et al. 2015, ApJ, 808, 184
Murphy, K. D., & Yaqoob, T. 2009, MNRAS, 397, 1549
Nandra, K., & Pounds, K. A. 1994, MNRAS, 268, 405
Page, M. J., Loaring, N. S., Dwelly, T., et al. 2006, MNRAS, 369, 156
Petric, A. O., Armus, L., Howell, J., et al. 2011, ApJ, 730, 28
Pope, A., Bussmann, R. S., Dey, A., et al. 2008, ApJ, 689, 127
Pozzi, F., Vignali, C., Gruppioni, C., et al. 2012, MNRAS, 423, 1909
Ricci, C., Bauer, F. E., Treister, E., et al. 2017, MNRAS, 468, 1273
Ricci, C., Ueda, Y., Koss, M. J., et al. 2015, ApJL, 815, L13
Rigby, J. R., Diamond-Stanic, A. M., & Aniano, G. 2009, ApJ, 700, 1878
Riguccini, L., Le Floc'h, E., Ilbert, O., et al. 2011, A&A, 534, A81
Riguccini, L., Le Floc'h, E., Mullaney, J. R., et al. 2015, MNRAS, 452, 470
Roseboom, I. G., Oliver, S. J., Kunz, M., et al. 2010, MNRAS, 409, 48
Salvato, M., Hasinger, G., Ilbert, O., et al. 2009, ApJ, 690, 1250
Sanders, D. B. 1999, Ap&SS, 266, 331
Sani, E., Lutz, D., Risaliti, G., et al. 2010, MNRAS, 403, 1246
Suh, H., Civano, F., Hasinger, G., et al. 2017, ApJ, 841, 102
Symeonidis, M. 2017, MNRAS, 465, 1401
Symeonidis, M., Giblin, B. M., Page, M. J., et al. 2016, MNRAS, 459, 257
Tacconi, L. J., Genzel, R., Saintonge, A., et al. 2018, ApJ, 853, 179
Tozzi, P., Gilli, R., Mainieri, V., et al. 2006, A&A, 451, 457
Treister, E., Cardamone, C. N., Schawinski, K., et al. 2009a, ApJ, 706, 535
Treister, E., & Urry, C. M. 2005, ApJ, 630, 115
Treister, E., Urry, C. M., Chatzichristou, E., et al. 2004, ApJ, 616, 123
Treister, E., Urry, C. M., Schawinski, K., Cardamone, C. N., & Sanders, D. B. 2010, ApJL, 722, L238
Treister, E., Urry, C. M., Van Duyne, J., et al. 2006, ApJ, 640, 603
Treister, E., Urry, C. M., & Virani, S. 2009b, ApJ, 696, 110
Ueda, Y., Akiyama, M., Hasinger, G., Miyaji, T., & Watson, M. G. 2014, ApJ, 786, 104
Ueda, Y., Akiyama, M., Ohta, K., & Miyaji, T. 2003, ApJ, 598, 886
Vasudevan, R. V., & Fabian, A. C. 2009, MNRAS, 392, 1124
Whitaker, K. E., van Dokkum, P. G., Brammer, G., & Franx, M. 2012, ApJL, 754, L29
Willingale, R., Starling, R. L. C., Beardmore, A. P., Tanvir, N. R., & O'Brien, P. T. 2013, MNRAS, 431, 394
Worsley, M. A., Fabian, A. C., Bauer, F. E., et al. 2005, MNRAS, 357, 1281